ACS APPLIED MATERIALS & INTERFACES

Research Article

www.acsami.org

Quasi-Photonic Crystal Effect of $TiCl_3$/Electrolyte Matrix in Unipolar Dye–Absorber Devices

Dong-Won Park,[†] Yonkil Jeong,*[,†] Thangapandi PremKumar,[†] and Jaeyoung Lee*[,†,‡,§]

[†]Research Institute for Solar and Sustainable Energies, [‡]School of Environmental Science and Engineering and [§]Ertl Center for Electrochemistry and Catalysis, Gwangju Institute of Science Technology, Gwangju 500-712, South Korea

ABSTRACT: Effectiveness of $TiCl_3$ pre- and post-treatments on dye-sensitized solar cells (DSCs) and interfacial charge-transfer properties were investigated. It was confirmed that a yield of current collection was strongly dependent on the position of the $TiCl_3$/electrolyte matrix in the DSC configuration. The interfacial charge-transfer properties were studied using thermionic emission–diffusion process and electrochemical impedance spectroscopy analysis. The $TiCl_3$/electrolyte matrix was considered to be a three-dimensional quasi-photonic crystal with a photonic band gap, which reinforces electric field and facilitates current collection from the $TiCl_3$/electrolyte matrix to the FTO by accelerating electron motion, whereas the potential barrier blocks current collection from the TiO_2 bulk region to the FTO and decreases current.

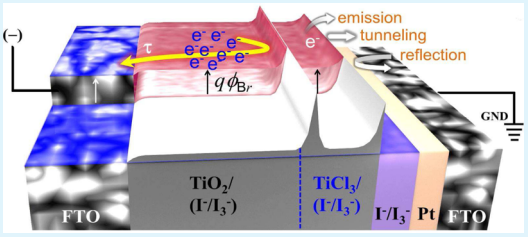

KEYWORDS: *$TiCl_3$/electrolyte matrix, light-scattering layer, interfacial charge-transfer loss, dye-sensitized solar cell, photonic crystal*

INTRODUCTION

Interfacial properties of heterojunction devices have been enormously issued and studied. In particular, study on the interfacial charge-transfer characteristics between solid state semiconductors and liquid state electrolytes such as dye-sensitized solar cells (DSCs), which are almost one kind of the unipolar absorber devices, is still issuable hermeneutically and helpful to trace mechanism. In the DSCs, the solid state semiconductors consist of an additional TiO_2 compact layer prepared by pretreatment on fluorine-doped SnO_2 (FTO) glass and TiO_2 mesoporous layer by post-treatment with an aqueous solution of titanium precursor.[1−9] These treatments are mainly focused on reduction of charge carrier recombination and light-scattering effect; it is known that the pretreatment practically influences the adhesion between the FTO substrate and the porous TiO_2 layer and prevents the charge-transfer loss caused by recombination between electrons deriving from the FTO and the I_3^- ions in the redox electrolyte.[3,10,11] The post-treatment serves as a light-scattering layer that can enhance electron injection efficiency and consequently improve the photocurrent. The generally fabricated TiO_2 mesoporous layer thickness by post-treatment is in the range of a few micrometers to within 10 μm, and consequently, absorption probability is enhanced due to an increased optical path length by diffuse random scattering of incident light into the thick bulk layer. The TiO_2 mesoporous layer by post-treatment can be fabricated by various methods such as hydrolysis, sputtering, chemical bath deposition, electrodeposition, and spin coating.[12−18,20,21] The growth method by hydrolysis of $TiCl_4$ is often employed to fabricate the TiO_2 light-scattering layer owing to its simple and inexpensive method, whereas aqueous solutions of $TiCl_4$ are conventionally prepared under ice-cooled conditions, and relatively it is not preferable for simplicity of the fabrication process.[7,23] Alternatively, a $TiCl_3$ treatment has been employed, and its effectiveness also has been confirmed for overall device performance.[24] As described above, pretreatment and the post-treatment are utilized for the recombination preventing layer and the scattering layer for electron injection efficiency enhancement, respectively. There are two major loss factors such as intrinsic and extrinsic losses. Extrinsic losses can be reduced using macroscopic engineering, whereas the intrinsic losses give birth to many mechanisms and issues. The intrinsic losses such as Boltzmann, thermalization, and band gap losses represent fundamental limitations of energy conversion with a given operating principle.[25] From the point of view of intrinsic properties such as negative and/or assistive electron behaviors between adjacent layers, treatment of $TiCl_4$ and $TiCl_3$ is necessary to be further discussed using a conventional idea of device physics, which can simplify physicochemical factors and facilitate device design through intuitive analysis.

In this article, our concerns are mainly focused on fabrication of an advanced light steering layer with submicrometer thickness using a simple $TiCl_3$ treatment and its interfacial charge-transfer properties between the adjacent layers of the fabricated TiO_2 layer derived from $TiCl_3$, which is abbreviated to the $TiCl_3$ layer for convenience. Three types of device configurations are fabricated as shown in Figure 1. The methods used in this treatment include $TiCl_3$ electrodeposition, titanium isopropoxide alcoholysis, and titanium tetrachloride ($TiCl_4$) hydrolytic reactions.[16−18,24,26] We show that the effectiveness of the thin $TiCl_3$ layer is comparable and/or

Received: June 11, 2014
Accepted: July 29, 2014
Published: July 29, 2014

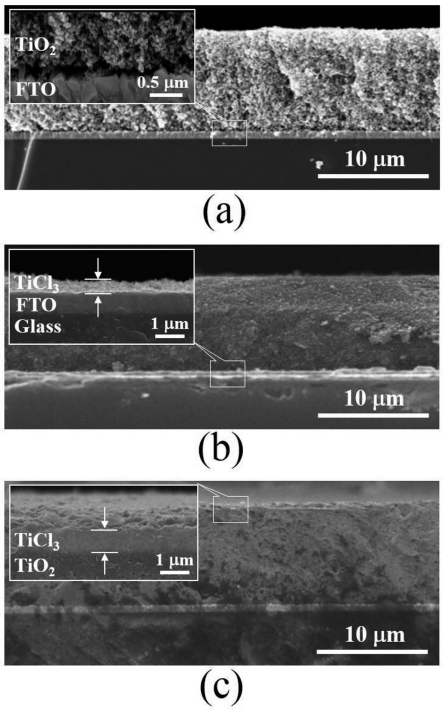

Figure 1. SEM images of the conventional porous TiO_2/FTO/Glass structure (a), the porous TiO_2/$TiCl_3$/FTO/Glass structure (b), and the $TiCl_3$/porous TiO_2/FTO/Glass structure (c). Inset in a displays a magnified interface between the porous TiO_2 and the FTO. Insets in b and c display the magnified interfaces between the adjacent $TiCl_3$ layers.

superior to that of the conventional $TiCl_4$ treatment as reported. We trace additional information for the $TiCl_3$/electrolyte matrix, which induces photonic band gap and reinforces electric field, using a thermionic emission−diffusion (TED) process and electrochemical impedance spectroscopy (EIS) analysis. It is newly suggested that the fabricated $TiCl_3$/electrolyte matrix serves as a three-dimensional quasi-photonic crystal.

EXPERIMENTAL SECTION

To investigate the effectiveness of the TiO_2 layer derived from $TiCl_3$ (abbreviated to the $TiCl_3$ layer) on DSC devices, three types of DSCs were fabricated as shown in Figure 1. Titanium(III) chloride ($TiCl_3$), lithium iodide (LiI), and 4-*tert*-butylpyridine (4-tbp) were obtained from Aldrich. 1,2-Dimethyl-3-propylimidazolium iodide (DMPII) and 3-methoxypropionitrile were purchased from Solaronix. To make the DSC photoelectrodes, the FTO glass with a sheet resistance of 12 Ω cm^{-2} (Asahi glass Co., Japan) was cleaned with ethanol and deionized (DI) water using ultrasonication for each 10 min. After treatment in a UV−O_3 system for 18 min, the TiO_2 paste was then coated by squeeze printing and sintered at 500 °C for 1 h, resulting in a TiO_2 layer containing ca. 20 nm sized particles of around 10 μm thickness (Figure 1a). The $TiCl_3$ layer was prepared by the following process; the FTO glass was immersed into 40 mM $TiCl_3$ aqueous solution at 70 °C for 30 min and rinsed with DI water and anhydrous ethanol. After drying at room temperature for 5 min, a layer of the TiO_2 paste was coated on the $TiCl_3$ layer by squeeze printing and sintered at 500 °C for 1 h. (Figure 1b). For the Figure 1c structure, the TiO_2-coated electrodes were immersed into a 40 mM $TiCl_3$ aqueous solution as described above and then sintered at 500 °C for 1 h. For a reference, $TiCl_4$ treatment was carried out by immersing the TiO_2-coated electrode in a 40 mM $TiCl_4$ (aq) at 70 °C for 30 min, rinsed with DI water and anhydrous ethanol, and sintered at 500 °C for 30 min. DSC devices were fabricated as reported in the literature using N719 dye (Solaronix, 5×10^{-4} M) as a photosensitizer.[20,21] The fabricated single TiO_2 layer and TiO_2 layer combined with the $TiCl_3$ layer were sandwiched with Pt counter electrode deposited on the FTO. The electrolyte was composed of 0.5 M LiI, 0.05 M I_2, 0.6 M DMPII, and 0.5 M 4-tbp in 3-methoxypropionitrile. The selected active area was 0.25 cm^2, and the cell edges were sealed with Surlyn (Dupont, grade 1702). Field emission scanning electron microscopy (SEM; S-4700, Hitachi) was used to characterize the morphology of the interface between the TiO_2 and the $TiCl_3$ layers. Transmittance spectra of the samples were measured with a UV−vis−NIR spectrometer (Varian Cary 5000). The full cell configuration was made by a simple attachment with an additional FTO glass, and the electrolyte was injected into the sandwiched structures for measurement of current−voltage (J−V), external quantum efficiency (EQE), and EIS. Solar cell efficiencies were measured and recorded using a Keithley 4300 source meter under 100 mW cm^{-2} irradiation (Oriel Sol3A, 450-W solar simulator equipped with an AM 1.5-G filter; Oriel Instruments, Irvine, CA, USA). The EQE was recorded in the wavelength region from 300 to 800 nm using incident-photon-to-current efficiency measurement apparatus (QEX7, PV Measurements). EIS measurements were performed using the ac impedance (CHI 660A, USA) over a frequency range of 1 to 10^6 Hz with amplitudes of ±5 mV over the V_{oc}. All materials fabrication and device characterization were statistically carried out and analyzed.[27,28]

RESULTS AND DISCUSSION

Figure 1 shows the SEM images of the conventional porous TiO_2/FTO/Glass structure (a), the porous TiO_2/$TiCl_3$/FTO/Glass structure (b), and the $TiCl_3$/porous TiO_2/FTO/Glass structure (c). The compact $TiCl_3$ layer is confirmed in the contrast difference of the inset images. The inset in Figure 1b is an image before porous TiO_2 fabrication. The thickness of the deposited $TiCl_3$ layer is around 0.6 μm for Figure 1b and around 0.9 μm for Figure 1c. The fabricated structures are employed to the DSC device fabrications, and each structure corresponds to the A, B, and C devices, respectively.

Figure 2 shows the transmittance spectra of the fabricated sample a, b, and c structures as shown in Figure 1. Here the

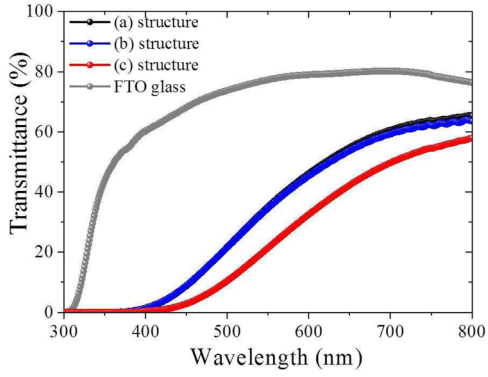

Figure 2. Transmittance spectra of the conventional porous TiO_2/FTO/Glass structure (a), the porous TiO_2/$TiCl_3$/FTO/Glass structure (b), the $TiCl_3$/porous TiO_2/FTO/Glass structure (c), and the FTO/Glass substrate.

light was incident from the FTO glass. The transmittance spectra of the a and b structures are almost similar, whereas the c structure exhibits the transmittance loss of about 10%, compare to those of the a and b structures in the wavelength region from 500 to ~800 nm. The transmittance loss of the c structure can be attributed to an abrupt change of the refractive index (n) between the $TiCl_3$ layer and air. The n of the $TiCl_3$ layer is estimated to be around 1.85 ± 0.1, and that of the air is

well known to be around 1.0.[29] In the beginning, the incident light direction to the glass ($n \approx 1.5$) is abruptly refracted and slowly changed because the refractive indices of the FTO ($n \approx 1.7$), the TiO_2 layer ($n \approx 1.8$), and the $TiCl_3$ layer ($n = 1.85 \pm 0.1$) are similar to each other, where n of the TiO_2 layer is an assumption from the n of the TiO_2/dye/electrolyte layer.[30] The traveling light through the $TiCl_3$ layer can be abruptly refracted or reflected into the TiO_2 layer; although the difference of refractive indices between the TiO_2 layer and the $TiCl_3$ layer is small, a sequential increase of the refractive indices increases the probability of total reflection into the TiO_2 layer at the interface between the $TiCl_3$ layer and air, with a long pathway where the thickness of the $TiCl_3$ layer is much higher than that of the b structure as shown in Figure 1. In the case of the b structure the $TiCl_3$ layer is sandwiched between the FTO and the TiO_2 layer. The traveling light direction can be slightly distorted, and the probability of the total reflection can be reduced compared to the c structure with a rather shallow thickness. Hence, the similar transmittance behavior of the a and b structures is reasonable.

Figure 3 shows the EQE (Figure 3a) and $J-V$ characteristic curves (Figure 3b) of the fabricated devices. For reference, a DSC device using a $TiCl_4$ post-treatment (D device) was fabricated and its device configuration is the same as that of the C device. The $J-V$ characteristic curve trace was carried out using a numerical calculation to investigate diode characteristics under illumination, and the parameters are summarized in Table 1. The best performance was achieved by the C device: a short-circuit current density (J_{sc}) of 18.35 mAcm^{-2}, an open-circuit voltage (V_{oc}) of 0.68 V, a fill factor (FF) of 58.0%, and an efficiency (Eff) of 7.2%. In Figure 2a, the EQE characteristic of the C device is in sharp contrast with that of the B device. In addition, the EQE characteristic of the B device is lower than that of the A device, which does not correspond to the transmittance behavior as shown in Figure 2. On the basis of the transmittance and our expectation, the EQE characteristic of the B device should shows a similar characteristic with that of the A device. This mismatch originates from the full cell configuration, and the EQE trend seems to be plausible to follow the scattering effect. However, we consider that the simple scattering effect is not suitable to explain fully the EQE trend in the complicated $TiCl_3$/electrolyte system. It should be noted that the reduction of the overall quantum efficiency is caused by light reflection and charge-transfer loss, where the reflection is a major extrinsic loss factor in general.[31] We will discuss charge transfer loss properties by introducing a charge-transfer loss factor (CTLF, α) and electron lifetime induced from the EIS. In the following we will introduce a modified concept of the scattering effect using the interface properties inspired by the electron lifetime and CTLF approach. In Figure 2, the overall device performance of the C device is higher than that of the reference D device and the higher performance of the C device is in good agreement with the previous report.[24] Performance parameters such as V_{oc} and FF are degraded except J_{sc} for the C device compared with that of the conventional A device. In general, V_{oc} and FF are directly related to the junction properties of devices because the V_{oc} is a function of a reverse saturation current density (J_0) mainly as a dark current in diode characteristics. The FF involves complex information including the junction properties and the series resistance. In our previous reports[20−22] the CTLF was extracted from the $J-V$ characteristic curve trace using the TED process, and the summarized expression is as follows

$$\alpha = \frac{J_0 \times 100}{mAT^2 e^{-qV_{oc}/kT}} \quad (1)$$

where the m^* is the effective mass of an electron, A is the Richardson constant of 1.2×10^5 mA cm^{-2} K^{-2} for a free electron, T is the absolute temperature, and kT/q is the thermal voltage. In this calculation, the effective mass factor of 10 was employed for an anatase TiO_2 semiconductor. The extracted CTLF has a physical quantity equivalent to a dominant electron lifetime (τ) with time dimension (ms) between the solid semiconductor and liquid electrolyte. The CTLF indicates

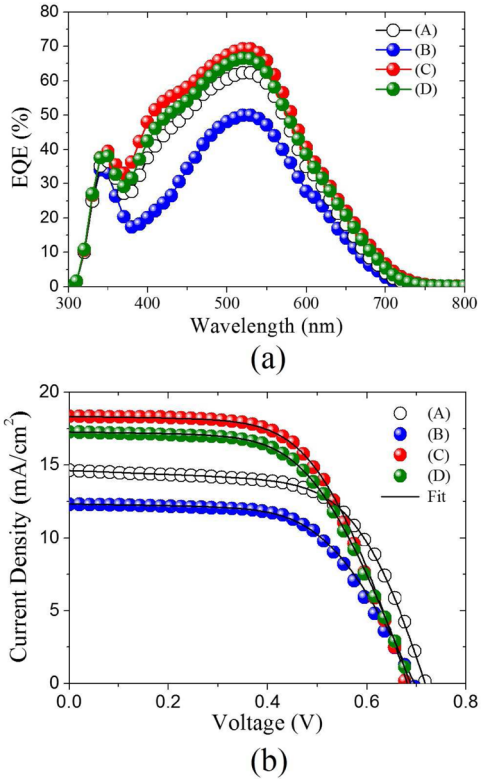

Figure 3. EQE (a) and experimental (shapes) and curve tracing (solid lines) of $J-V$ characteristics (b) of the fabricated devices.

Table 1. Parameters Experimentally Obtained from the $J-V$ Characteristic Curves and Parameters Extracted from Numerical Calculations

	experimental parameters				calculated results		
device	V_{oc} (V)	J_{sc} (mA/cm^2)	FF (%)	Eff (%)	J_0 (mA/cm^2)	CTLF (ms)	EIS, τ (ms)
A	0.72	14.65	61.0	6.4	1.4×10^{-5}	15.3	16.2
B	0.69	12.35	60.0	5.1	5.0×10^{-5}	17.2	19.6
C	0.68	18.35	58.0	7.2	6.0×10^{-5}	14.0	13.9
D	0.69	17.28	58.0	6.9	4.2×10^{-5}	14.4	

charge-transfer loss mechanisms such as thermionic emission, quantum mechanical tunneling, and quantum mechanical reflection. The τ is usually obtained from the EIS measurements and recognized as an important device quality factor. The CTLF calculated from the simple $J-V$ characteristic curve trace can help for finding the electron lifetime roughly because a simple prediction method can facilitate device design through intuitive analysis. We show that the calculated CTLF values are in good agreement with τ obtained from the EIS measurements in the next section.

Figure 4 shows the Nyquist plots obtained from the EIS and curve tracing and normalized loss factors of the devices.

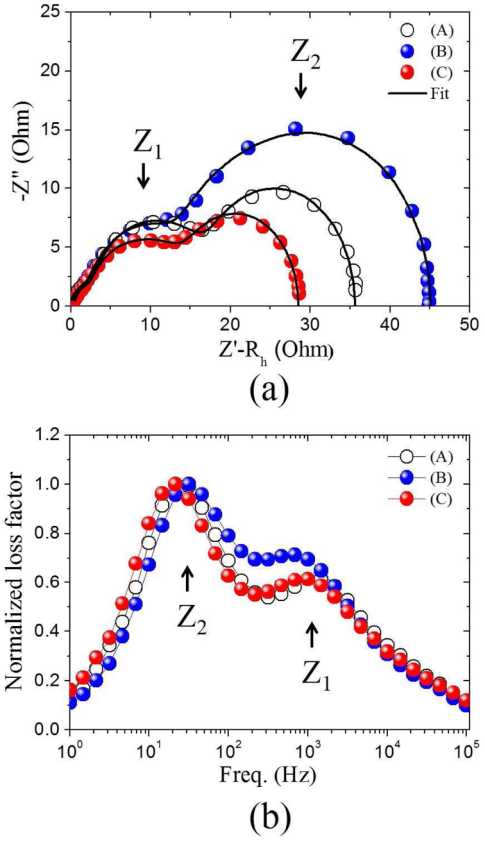

Figure 4. Nyquist plots (shapes) and curve tracing (solid lines) (a) and normalized loss factors (b) of the fabricated devices.

Analysis of the Nyquist plots and normalized loss factors are well described in the literature including our previous work.[19−21,31] Parameters Z_1 and Z_2 represent the impedance related to charge transport at the Pt counter electrode in the high-frequency region and the impedance related to that at the interface between the TiO_2 or $TiCl_3$ layer and the electrolyte in the middle-frequency region, respectively. Intuitively, it is found that the series resistance of the C device is lower than those of the other devices observing the Z_1 region. On the other hand, the junction properties are prominent in the Z_2 region; in particular, the Z_2 region of the B device reveals an abnormally enlarged semicircle compared to the other devices. Using the simple resistance−capacitance (RC) circuit model, the experimentally obtained Nyquist curves were precisely traced.[19,20] The real parts of impedance except the resistance of the transparent conducting oxide layer (R_h) are generally expressed to the following form

$$Z' - R_h = \frac{R}{1 + \omega^2 C^2 R^2} \quad (2)$$

where R is the charge-transfer resistance, C is the capacitance, and ω is the angular frequency.

$$Z' - R_h = Z_1' + Z_2' = Z_1' + \left(\frac{18.8}{1 + \omega^2(8.6 \times 10^{-4})^2 \times 18.8^2}\right) \quad (3)$$

$$Z' - R_h = Z_1' + Z_2' = Z_1' + \left[\left(\frac{10.0}{1 + \omega^2(7.0 \times 10^{-4})^2 \times 10.0^2}\right) + \left(\frac{21.8}{1 + \omega^2(9.0 \times 10^{-4})^2 \times 21.8^2}\right)\right] \quad (4)$$

$$Z' - R_h = Z_1' + Z_2' = Z_1' + \left(\frac{14.5}{1 + \omega^2(9.6 \times 10^{-4})^2 \times 14.5^2}\right) \quad (5)$$

The calculated forms in eqs 3, 4, and 5 are the mathematical expressions for the A, B, and C devices, respectively. The mathematical expression of the real part for the Z_1 region is omitted because our concern is in the junction interface related with the Z_2 region. Equations 3 and 5 are expressed to only one RC circuit, while eq 4 is expressed to a combination of two RC circuits. From eqs 3, 4, and 5 the dominant RC time constants of 16.2, 19.6, and 13.9 ms are obtained, respectively. The RC time constants are regarded as the τ, and these values are almost in good agreement with the CTLF values obtained from the simple $J-V$ characteristic curve trace as shown in Table 1. For eq 4 the τ of 7.0 ms is another residual loss factor within the B device.

The τ of the B device is the highest, whereas its overall device performance is lowest. The τ is the device quality factor between the solid semiconductor and liquid electrolyte as described above, whereas an assistive or lossy electron behavior influencing τ depends on a specific region in the device configuration. Figure 5 illustrates the total concepts in this work, including the different energy structures. In Figure 5a, the incident light is absorbed into the porous TiO_2 with dye adsorption except the infrared transmission. The obtained 16.2 ms is the τ at the interface between the porous TiO_2 and the electrolyte adjacent the FTO because the electron can be easily swept away into the adjacent FTO. The energy structure in Figure 5a illustrates the equilibrium state under no illumination (conduction band E_c plane and Fermi level E_f are aligned) and the nonequilibrium state under illumination with forward bias (quasi-Fermi level splitting E_{fn}). The interface between the TiO_2 and the electrolyte forms the Schottky barrier height, and the barrier height is reduced as much as $q\phi_{Br}$, which is converted to the output voltage of V_{oc} under illumination. The obtained τ of 16.2 ms is equivalent to the charge-transfer losses, which consist of the thermionic emission, quantum mechanical tunneling, and quantum mechanical reflection as illustrated in the energy structure in Figure 5a. In Figure 5b, the light is reflected in the $TiCl_3/(I^-/I_3^-)$ matrix. From the point of view that photonic crystals should have a periodic potential or a periodic dielectric material, a dielectric periodicity of the $TiCl_3/(I^-/I_3^-)$ matrix may have arguable points. However, we

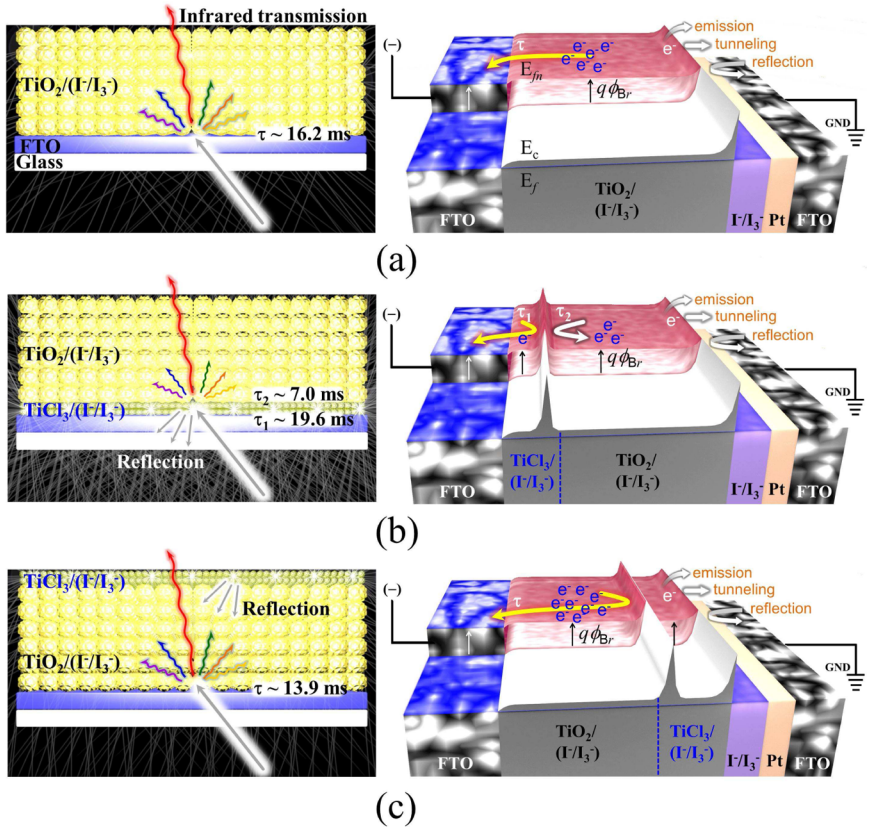

Figure 5. Schematics of the TiO_2/FTO (a), TiO_2/$TiCl_3$/FTO (b), and $TiCl_3$/TiO_2/FTO (c) configurations. DSC devices fabricated using the configurations have the equilibrium energy state (conduction band E_c plane and Fermi level E_f are aligned) under no illumination and the nonequilibrium energy state (quasi-Fermi level splitting E_{fn} plane) under illumination with a forward bias as illustrated. $TiCl_3/(I^-/I_3^-)$ matrix serves as a three-dimensional quasi-photonic crystal with a photonic band gap, which correspond to the UV–vis frequencies with a partial discontinuity of the wave vector. $TiCl_3/(I^-/I_3^-)$ matrix creates a potential barrier, which reinforces the electric field and accelerates electron motion, whereas the potential barrier depends on the device configuration, which determines the overall device performance. The degraded interfacial charge transport characteristics caused by the $TiCl_3/(I^-/I_3^-)$ matrix originate from the thermionic emission–diffusion process, which indicates charge-transfer loss mechanisms such as electron emission, tunneling, and reflection.

consider that the $TiCl_3/(I^-/I_3^-)$ matrix consists of random clusters with a high dielectric $TiCl_3$ and a low dielectric (I^-/I_3^-), which serve as a three-dimensional quasi-photonic crystal. In the $TiCl_3/(I^-/I_3^-)$ matrix, a photonic band gap can be formed and correspond to the UV–vis frequencies with a partial discontinuity of the wave vector on the basis of the photonic crystal principle. The colloidal $TiCl_3$ particles are enough to create a large band gap compared to the conventional TiO_2 band gap; the smaller particle size increases an intraband transition gap. The photonic band gap in the $TiCl_3/(I^-/I_3^-)$ matrix can be identified to the increased intraband transition gap. The energy structure in Figure 5b illustrates a large potential barrier of the $TiCl_3/(I^-/I_3^-)$ matrix. The obtained residual low τ_2 of 7.0 ms can be attributed to the fact that the photoexcited carriers in the bulk TiO_2 region cannot be collected to the FTO by the potential barrier. The obtained 19.6 ms is the τ_1 at the interface between the $TiCl_3/(I^-/I_3^-)$ matrix and the FTO. The photoexcited carriers in the $TiCl_3/(I^-/I_3^-)$ matrix are rapidly swept away into the FTO because the potential barrier reinforces electric field and accelerates electron motion. In Figure 5c, the obtained τ of 13.9 ms is due to the interface between the porous TiO_2 and the FTO. The photoexcited carriers at the adjacent $TiCl_3/(I^-/I_3^-)$ matrix are assisted by the electric field induced from the potential barrier, whereas the electron traveling pathway up to the FTO is relatively long, and the probability of charge-transfer loss is high.

CONCLUSIONS

The effectiveness of $TiCl_3$ pre- and post-treatments on the DSC devices and the interfacial charge-transfer properties were investigated. It was newly suggested that the $TiCl_3/(I^-/I_3^-)$ matrix serves as a three-dimensional quasi-photonic crystal with a photonic band gap, which corresponds to the UV–vis frequencies with a partial discontinuity of the wave vector. The photonic band gap and increased intraband transition gap in the $TiCl_3/(I^-/I_3^-)$ matrix are identified to each other. The $TiCl_3/(I^-/I_3^-)$ matrix formed by $TiCl_3$ pretreatment creates a potential barrier, which reinforces the electric field and facilitates current collection from the $TiCl_3/(I^-/I_3^-)$ matrix to the FTO by accelerating electron motion, whereas the potential barrier blocks current collection from the TiO_2 bulk region to the FTO and decreases current. The $TiCl_3/(I^-/I_3^-)$ matrix formed by the $TiCl_3$ post-treatment improves the UV–vis absorption by reflection and boosts current, whereas the potential barrier degrades charge transport characteristic at the interface between the $TiCl_3/(I^-/I_3^-)$ matrix and the bulk electrolyte. We consider that the degraded interfacial charge transport mechanism originates from the thermionic emission–diffusion process. Except the current boosting by the

improvement of the UV−vis absorption, the pre- and post-treatments degrade the overall device performance. The advanced device design is required using the trade-off methods; for example, reduction of a well-defined $TiCl_3$ layer thickness can control both the reflection and the interfacial charge transport characteristics and extract maximum performance. Additionally, the expected quasi-photonic crystal effect can be tuned or modified by controlling the particle size of the $TiCl_3$ or replacing electrolyte.

AUTHOR INFORMATION

Corresponding Authors

*E-mail: yjeong@gist.ac.kr.
*E-mail: jaeyoung@gist.ac.kr.

Notes

The authors declare no competing financial interest.

ACKNOWLEDGMENTS

This work was supported by the Core Technology Development Program for Next-generation Solar Cells of Research Institute for Solar and Sustainable Energies (RISE), GIST.

REFERENCES

(1) Nazeeruddin, M. K.; Kay, A.; Rodicio, I.; Humphry-Baker, R.; Müller, E.; Liska, P.; Vlachopoulos, N.; Grätzel, M. Conversion of Light to Electricity by *cis*-X_2Bis(2,2′-bipyridyl-4,4′-dicarboxylate)-ruthenium(II) Charge-Transfer Sensitizers (X = Cl^-, Br^-, I^-, CN^-, and SCN^-) on Nanocrystalline TiO_2 Electrodes. *J. Am. Chem. Soc.* **1993**, *115*, 6382−6390.

(2) Barbe, C. J.; Arendse, F.; Comte, P.; Jirousek, M.; Lenzmann, F.; Shklover, V.; Grätzel, M. Nanocrystalline Titanium Oxide Electrodes for Photovoltaic Applications. *J. Am. Ceram. Soc.* **1997**, *80*, 3157−3171.

(3) Ito, S.; Liska, P.; Comte, P.; Charvet, R.; Péchy, P.; Bach, U.; Schmidt-Mende, L.; Zakeeruddin, S. M.; Kay, A.; Nazeeruddin, M. K.; Grätzel, M. Control of Dark Current in Photoelectrochemical (TiO_2/I^-−I_3^-) and Dye-Sensitized Solar Cells. *Chem. Commun.* **2005**, *34*, 4351−4353.

(4) Wei, M.; Konishi, Y.; Zhou, H.; Yanagida, M.; Sugihara, H.; Arakawa, H. Highly Efficienct Dye-Sensitized Solar Cells Composed of Mesoporous Titanium Dioxide. *J. Mater. Chem.* **2006**, *16*, 1287−1293.

(5) O'Regan, B. C.; Durrant, J. R.; Sommeling, P. M.; Bakker, N. J. Influence of the $TiCl_4$ Treatment on Nanocrystalline TiO_2 Films in Dye-Sensitized Solar Cells. 2. Charge Density, Band Edge Shifts, and Quantification of Recombination Losses at Short Circuit. *J. Phys. Chem. C* **2007**, *111*, 14001−14010.

(6) Vesce, L.; Riccitelli, R.; Soscia, G.; Brown, T. M.; Carlo, A. D.; Reale, A. Optimization of Nanostructured Titania Photoanodes for Dye-Sensitized Solar Cells: Study and Experimentation of $TiCl_4$ Treatment. *J. Non-Cryst. Solids* **2010**, *356*, 1958−1961.

(7) Kim, D.; Roy, P.; Lee, K.; Schmuki, P. Dye-Sensitized Solar Cells using Anodic TiO_2 Mesosponge: Improved Efficiency by $TiCl_4$ Treatment. *Electrochem. Commun.* **2012**, *12*, 574−578.

(8) Huang, N.; Liu, Y.; Peng, T.; Sun, X.; Sebo, B.; Tai, Q.; Hu, H.; Chen, B.; Guo, S. S.; Zhao, X. Synergistic Effects of ZnO Compact Layer and $TiCl_4$ Post-Treatment for Dye-Sensitized Solar Cells. *J. Power Sources* **2012**, *204*, 257−264.

(9) Chou, C. S.; Guo, M. G.; Liu, K. H.; Chen, Y. S. Preparation of TiO_2 Particles and Their Applications in the Light Scattering Layer of a Dye-Sensitized Solar Cell. *Appl. Energy* **2012**, *92*, 224−233.

(10) Cameron, P. J.; Peter, L. M. How Does Back-Reaction at the Conducting Glass Substrate Influence the Dynamic Photovoltage Response of Nanocrystalline Dye-Sensitized Solar Cells? *J. Phys. Chem. B* **2005**, *109*, 7392−7398.

(11) Macak, J. M.; Tsuchiya, H.; Taveira, L.; Aldabergerova, S.; Schmuki, P. Smooth Anodic TiO_2 Nanotubes. *Angew. Chem., Int. Ed.* **2005**, *44*, 7463−7465.

(12) Peng, B.; Jungmanna, G.; Jäger, C.; Haarer, D.; Schmidt, H. W.; Thelakkat, M. Systematic Investigation of the Role of Compact TiO_2 Layer in Solid State Dye-Sensitized TiO_2 Solar Cells. *Coord. Chem. Rev.* **2004**, *248*, 1479−1489.

(13) Hore, S.; Kern, R. Implication of Device Functioning due to Back Reaction of Electrons via the Conducting Glass Substrate in Dye Sensitized Solar Cells. *Appl. Phys. Lett.* **2005**, *87*, 263504.

(14) Hattori, R.; Goto, H. Carrier Leakage Blocking Effect of High Temperature Sputtered TiO_2 Film on Dye-Sensitized Mesoporous Photoelectrode. *Thin Solid Films* **2007**, *515*, 8045−8049.

(15) Yu, H.; Zhang, S.; Zhao, H.; Will, G.; Liu, P. An Efficient and Low-Cost TiO_2 Compact Layer for Performance Improvement of Dye-Sensitized Solar Cells. *Electrochim. Acta* **2009**, *54*, 1319−1324.

(16) Park, K.; Zhang, Q.; Garcia, B. B.; Zhou, X.; Jeong, Y. H.; Cao, G. Effect of an Ultrathin TiO_2 Layer Coated on Submicrometer-Sized ZnO Nanocrystallite Aggregates by Atomic Layer Deposition on the Performance of Dye-Sensitized Solar Cells. *Adv. Mater.* **2010**, *22*, 2329−2332.

(17) Park, D. W.; Choi, Y. K.; Hwang, K. J.; Lee, J. W.; Park, J. K.; Jang, H. D.; Park, H. S.; Yoo, S. J. Nanocrystalline TiO_2 Films Treated with Acid and Base Catalysts for Dye-Sensitized Solar Cells. *Adv. Powder Technol.* **2011**, *22*, 771−776.

(18) Ishida, M.; Park, S. W.; Hwang, D.; Koo, Y. B.; Sessler, J. L.; Kim, D. Y.; Kim, D. Donor-Substituted β-Functionalized Porphyrin Dyes on Hierarchically Structured Mesoporous TiO_2 Spheres. Highly Efficient Dye-Sensitized Solar Cells. *J. Phys. Chem. C* **2011**, *115*, 19343−19354.

(19) Han, L.; Koide, N.; Chiba, Y.; Mitate, T. Modeling of an Equivalent Circuit for Dye-Sensitized Solar Cells. *Appl. Phys. Lett.* **2004**, *84*, 2433−2435.

(20) Park, D. W.; Jeong, Y.; Lee, J.; Lee, J.; Moon, S. H. Interfacial Charge-Transfer Loss in Dye-Sensitized Solar Cells. *J. Phys. Chem. C* **2013**, *117*, 2734−2739.

(21) Park, D. W.; Jeong, Y.; Kumar, T. P.; Lee, J.; Choi, Y. K. Influence of Acid/Base Co-Catalyst on the Photoelectrochemical Properties of TiO_2 Thin Flms in Dye-Sensitized Solar Cells. *Electrochim. Acta* **2013**, *107*, 619−623.

(22) Sze, S. M. *Physics of Semiconductor Devices*, 2nd ed.; Wiley-Interscience: New York, 1981.

(23) Kim, S. J.; Park, S. D.; Jeong, Y. H.; Park, S. Homogeneous Precipitation of TiO_2 Ultrafine Powders from Aqueous $TiOCl_2$ Solution. *J. Am. Ceram. Soc.* **1999**, *82*, 927−932.

(24) Wu, M. S.; Tsai, C. H.; Jow, J. J.; Wei, T. C. Enhanced Performance of Dye-Sensitized Solar Cell via Surface Modification of Mesoporous TiO_2 Photoanode with Electrodeposited Thin TiO_2 Layer. *Electrochim. Acta* **2011**, *56*, 8906−8911.

(25) Nelson, C. A.; Monahan, N. R.; Zhu, X. Y. Exceeding the Shockley-Queisser limit in Solar Energy Conversion. *Energy Environ. Sci.* **2013**, *6*, 3508−3519.

(26) Tsai, T. Y.; Lu, S. Y. A Novel Way of Improving Light Harvesting in Dye-Sensitized Solar Cells − Electrodeposition of Titania. *Electrochem. Commun.* **2009**, *11*, 2180−2183.

(27) Luber, E. J.; Buriak, J. M. Reporting Performance in Organic Photovoltaic Devices. *ACS Nano* **2013**, *7*, 4708−4714.

(28) Schanze, K. S.; Mallett, J. J. Fifth Anniversary: A New Year and New Procedures. *ACS Appl. Mater. Interfaces* **2014**, *6*, 1−2.

(29) Baldini, G.; Pollini, I.; Spinolo, G. Optical Properties of α- and β- $TiCl_3$. *Phys. Status Solidi B* **1968**, *27*, 95−100.

(30) Wenger, S.; Schmid, M.; Rothenberger, G.; Gentsch, A.; Grätzel, M.; Schumacher, J. Coupled Optical and Electronic Modeling of Dye-Sensitized Solar Cells for Steady-State Parameter Extraction. *J. Phys. Chem. C* **2011**, *115*, 10218−10229.

(31) Nayak, P.; Bisquert, J.; Cahen, D. Assessing Possibilities and Limits for Solar Cells. *Adv. Mater.* **2011**, *23*, 2870−2876.